Identification of the friction under high pressure between an aggregate material and steel: Experimental and modelling aspects

Bastien Durand, Franck Delvare, Patrice Bailly, Didier Picart

Identification of the friction under high pressure between an aggregate material and steel: experimental and modelling aspects

Bastien Durand[1,2], Franck Delvare[3], Patrice Bailly[1] and Didier Picart[2]

[1]ENSI Bourges, Laboratoire PRISME, F-18020 Bourges, France

[2]CEA, DAM, Le Ripault, F-37260 Monts, France

[3]Université de Caen Basse-Normandie, UMR 6139 Laboratoire N. Oresme, F-14032 Caen, France

Abstract. The interface behaviour between steel and a quasi-brittle aggregate material is characterised up to normal pressures of the magnitude of 100MPa. This article presents a new test enabling the behaviour of the interface to be studied whilst retaining the sample's integrity. The experimental configuration having been retained consists in sliding a cylindrical sample of the material inside a steel tube, said tube acting both as a sliding surface and containment ring. The sample is pushed on one side and faces a spring on the other. The axial compression generates the interface pressure by Poisson effect. This originality of this assembly lies in the simultaneous application of normal pressure to the interface and of its relative motion. The assembly is placed in a quasi-static testing machine. The analysis is made by means of an analytical modelling of the test. This method enables the identification of the initial contact conditions (tightening of the sample), the friction coefficient and its dependence on the pressure. Numerical simulations of the test using a finite element method enables the analytical approach to be validated as well as the set of parameters identified depending on the normal pressure regimes.

1 Introduction

Certain dynamic tests enable the reactivity of compressed explosives (PBX) subjected to shocks to be tested. These are namely: the drop-weight test [8], the Steven-test [11], [24] and the Taylor shock test. The place and time of the priming of the chemical reaction particularly depend on the conditions of contact with the wall [5], [13], [20]. A numerical simulation of one variant of the Taylor test forms a simple illustration of the influence of the friction conditions upon ignition. This test consists in projecting a sample of explosive (cylindrical sample with a diameter and a height of 18mm) against a steel wall assumed to be pressure-resistant. The thermomechanical characteristics of PBX are given in [21]. Figure 1 shows the influence of the friction coefficient *f* on the maximal temperature reached by the sample during the impact. A very significant difference of around 200K is obtained between the two cases.

During an impact at these velocities, the normal contact pressures and the sliding velocities between steel and explosive are respectively of around 100MPa and 10 to 100m/s. Our aim is to recreate these velocity and pressure conditions, but in a configuration enabling the friction to be measured. Certain test benches partially fulfil this aim: tribometer with explosively-generated friction [17], target-projectile assembly with oblique impact [22], torsional Hopkinson bars [14], [15], [22], [23], dynamometrical ring with parallelepipedic sample launched by a gas cannon or by a hydraulic machine [19] and possibly pin on rotating disk [5].

For the sake of safety, the experiments are developed using an inert material, denoted I1. This material is namely a fine compressed powder (mixture of barium meal $BaSO_4$ -

29.3%wt -, of melanime -65.2%wt – and a binder -5.5%wt – made of an epoxy resin). Its mechanical behaviour closely resembles that of an explosive. This behaviour has previously been studied by carrying out triaxial compression tests [1]. Under compressive loading with high hydrostatic pressure (which is different from a purely hydrostatic loading), the material is able to flow when its plasticity threshold has been attained (here the maximal constraints obtained using triaxial tests are assimilated to a plasticity threshold in order to simplify the behaviour model). The plasticity threshold thus identified is of the Drucker-Prager type [1]. That is $\underline{\underline{\sigma}}$, P and σ_{mises} respectively the stress tensor, the hydrostatic pressure and the Von Mises equivalent stress:

(1) $$P = \frac{1}{3} tr\left(\underline{\underline{\sigma}}\right) \text{ and } \sigma_{mises} = \sqrt{\frac{3}{2}\left(\underline{\underline{\sigma}} - P\underline{\underline{I}}\right) : \left(\underline{\underline{\sigma}} - P\underline{\underline{I}}\right)}$$

where tr is the trace operator and $\underline{\underline{I}}$ the identity tensor. The criterion is thus given by the following formula:

(2) $$\sigma_{mises} - \alpha P < C$$

where the stress C depends on the strain rate. It equals 25MPa at low strain rates and exceeds 80MPa at those strain rates attained during compression tests on Hopkinson bars (typically $100s^{-1}$). The coefficient α is constant and equal to 0.64. In the event of uniaxial compressive loading, the criterion corresponds to a maximal acceptable stress of around 30MPa for low strain rates and around 100MPa for strain rates reached on Hopkinson bars [1].

One way of subjecting the interface to high pressures without fracturing the sample is to confine it. For this, a cylindrical sample of I1 is encased in a quasi-rigid tube. This

technique is employed to perform compression tests with quasi-uniaxial strain states [1], [9], [10]. Friction between the tube interface and the sample is here perceived as a drawback and has been studied in [3], [4], [27]. Since the mechanical behaviour of the tube is known, the strain measurements made by means of gauges glued to the external face enable the stresses on the interface to be measured. The idea retained is to slide the cylindrical sample into the tube, which acts as both a sliding surface and a confining vessel (given the Poisson effect of the sample). This principle has already been tested with a hollow sample, through whose length a tightening screw [6] passes. Despite the advantages of this principle, this first device does not allow the sample to be subjected to high pressures. The device being studied in this article allows us to overcome this drawback and to reach pressures of 100MPa at the interface. Our study here is limited to the cases of low relative velocities between the bearing faces.

The detailed description of the experimental configuration and the limits linked to the internal sliding are presented in section 2. A model enabling the identification of the friction parameters based on the measurements is described in section 3. The experimental results on the test examples using an inert material are then presented and analysed in section 4. Finally, section 5 focuses on validating the analysis method.

2 The experimental layout

2.1 The experimental device

The device proposed has been designed to reach high pressure levels. Before the test, the cylindrical sample is confined in a steel tube (c.f. Figure 2). It is pushed from top to

bottom by a mechanical machine. The movement of its base is countered by a spring assembly (of the Belleville type). The stiffness of the spring allows the value of the counter-pressure to be controlled. The originality of this assembly lies in that the normal pressure (by Poisson effect on the sample) and the sliding are imposed simultaneously. This allows the full pressure range to be covered, with the pressure gradually increasing along with the displacement. The inner wall of the steel tube was reamed and the sample was turned on a sliding lathe. Both have a weak surface roughness.

Figure 3 is a photograph of the device. For practical reasons, the confinement tube and the tube enclosing the spring may be screwed together. The parts belonging to such fastening system are neither shown nor modelled in the simulations by the finite element method mentioned in section 5.

The values of forces F_m and F_r are measured during the tests (c.f. Figure 4). F_m is the force exerted by the machine on the sample. It is given directly by the machine's force sensor. F_r is the force exerted by the aluminium rod on the sample. It is determined by the gauges glued to the rod.

Gauges are also glued to the external face of the confinement tube so as to measure the axial profile of the circumferential strain (c.f. Figure 2 and Figure 3).

2.2 Sliding without fracture

A prior study of the competition between internal sliding [26] and interfacial sliding is required to ensure the feasibility of this test. Indeed, further to a fracture, internal sliding of

the sample may well be obtained in addition to the sliding at the interface. Internal sliding may even be obtained with some extrusion of material between the tube and the upper piston.

A sliding state (i) described by Coulomb's law between the I1 sample and the tube and a quasi-uniaxial strain state (ii) are considered. The sample is assumed to remain in the elastic domain. On the interface, the stress tensor is of the following form:

$$\underline{\underline{\sigma}} = \begin{pmatrix} p & 0 & fp \\ 0 & p & 0 \\ fp & 0 & \frac{1-\nu}{\nu} p \end{pmatrix}_{r,\theta,z} \tag{3}$$

p being the interface pressure (positive compressive stresses), ν the Poisson coefficient of the material and f the friction coefficient at the interface. The expressions of the hydrostatic pressure P and the Von Mises stress σ_{mises} are deduced as follows:

$$\begin{cases} P = \frac{1+\nu}{3\nu} p \\ \sigma_{mises} = p\sqrt{\left(\frac{1-2\nu}{\nu}\right)^2 + 3f^2} \end{cases} \tag{4}$$

The equation (2) must be satisfied if the sample is not to be fractured. The limit friction coefficient may thus be defined as:

$$f_{\lim} = \sqrt{\frac{1}{3\nu^2}\left\{\left[\frac{\alpha(1+\nu)}{3}\right]^2 - (1-2\nu)^2\right\}} \tag{5}$$

If $f<f_{lim}$, the condition (2) is respected whatever the value of p. For $f>f_{lim}$, the condition (2) is respected if $p<p_{lim}$ with p_{lim} the limit pressure is defined by:

(6) $$p_{\lim} = \frac{C}{\sqrt{\left(\frac{1-2\nu}{\nu}\right)^2 + 3f^2} - \alpha\frac{1+\nu}{3\nu}}$$

p_{lim} depends on ν and α, but a minor variation of ν may have a great influence. Experimentally, the Poisson coefficient of the I1 is somewhere around 0.4. Figure 5 shows how this limit pressure varies as a function of ν and f. It is essential for the Poisson coefficient value ν to be known with suitable accuracy. It also shows that with a low Poisson coefficient value (0.38), pressures approaching 100MPa can be hoped for.

If $f>0.45$ is measured during the tests, it is almost certain that 100MPa will not be reached without fracturing the material. Naturally, in all cases, the samples must be checked a posteriori for any fractures.

3 Modelling of the test

3.1 The mechanical problem

The interface behaviour cannot be deduced by direct measurements. Indeed, a prior analysis of the test shows that the stress state at the interface is heterogeneous. A model must thus be established enabling this data to be acquired on the basis of measurements of F_m and F_r (c.f. Figure 6). For this, it is firstly necessary for the mechanical state of the sample to be determined.

Given that there is axial symmetry, the null components of the stress tensor $\underline{\underline{\sigma}}(r,z)$ are those indicated in relation (3). The corresponding strains are also null. The displacement is axisymmetrical, the radial (oriented by $\mathbf{u_r}$) and longitudinal (oriented by $\mathbf{u_z}$) components depend on r and z.

The sample is forced into the tube by using the testing machine. Because of the difference in diameters u_{ri}, the sample is subjected to pre-tightening linked to the radial displacement. If $u_r^{tube}(r=R,z)$ represents the radial displacement withstood by the tube at $r=R$, then we obtain:

(7) $$u_r(r=R,z) = u_r^{tube}(r=R,z) - u_{ri}$$

That is $p(z)$ and $\tau(z)$ the normal and tangential stresses at the interface (at $r=R$): $p(z)=\sigma_{rr}(r=R,z)$ and $\tau(z)=\sigma_{rz}(r=R,z)$. Conventionally, these are positive in compression.

Assuming that the friction at the interface is in accordance with Coulomb's law: the ratio of τ by p is equal to a coefficient f whose value is supposed to be little dependent on p. However, the pressure range covered during the experiments is far-reaching and possible dependence of the friction coefficient f at pressure p must be envisaged [2]. The retained hypothesis is that a small variation of f as a function of p may be approached by an affine function:

(8) $$\tau(z) = f(p(z)) \times p(z) \text{ with } f(p) = f_0(1-\beta p)$$

Forces F_m and F_r are expressed in terms of boundary conditions (at $z=0$ and at $z=L$):

(9) $$F_r = 2\pi\int_0^R r\sigma_{zz}(r, z=0)dr$$

(10) $$F_m = 2\pi\int_0^R r\sigma_{zz}(r, z=L)dr$$

Given the tube's thickness and the gap between the rigidities of the materials in contact, the confinement tube is very rigid compared with the sample. In this case, no coupling between the behaviours of the two solids is considered and the presence of the tube may be modelled by a boundary condition of the imposed displacement type. According to (7):

(11) $$u_r^{tube}(r=R, z)=0 \Rightarrow u_r(r=R, z)=-u_{ri}$$

In the event of there being no excess thickness in the assembly and when the friction coefficient is not dependent upon the pressure, a two-dimensional approximate solution may be established.

(12) $$u_{ri}=0 \Rightarrow u_r(r=R, z)=0$$

Assuming the sample is in an elastic state, the equilibrium equations, Hooke's law and the axial symmetry hypothesis are combined to produce the Navier equations:

(13) $$2(1-\nu)(r^2u_{r,rr}+ru_{r,r}-u_r)+r^2u_{z,rz}+r^2(1-2\nu)u_{r,zz}=0$$

(14) $$2(1-\nu)ru_{z,zz}+u_{r,z}+ru_{r,rz}+(1-2\nu)(u_{z,r}+ru_{z,rr})=0$$

The friction law imposes at $r=R$:

(15) $$2f\left[r(1-\nu)u_{r,r}+\nu u_r+r\nu u_{z,z}\right]+r(1-2\nu)(u_{r,z}+u_{z,r})=0$$

Since the sample is confined, the radial displacement and its variations are very low with respect to the other terms and a first order approximation consists in leaving out certain terms to eventually obtain the following relations:

(16) $$2(1-\nu)u_{r,rr}+u_{z,rz}=0$$

(17) $$2(1-\nu)ru_{z,zz}+(1-2\nu)(u_{z,r}+ru_{z,rr})=0$$

(18) $$2\nu f u_{z,z}+(1-2\nu)u_{z,r}=0 \text{ at } r=R$$

A solution is sought after in the following form:

(19) $$\begin{cases} u_r(r,z)=g(r)\psi(z) \\ u_z(r,z)=f(r)\varphi(z)+u_0 \end{cases}$$

In the event of f being low, the above hypothesis is verified (c.f. appendix), and the following solution may be found:

(20) $$\begin{cases} u_r = \dfrac{\nu f \varphi(0)}{R(1-\nu)^2} \exp\left(\dfrac{2\nu f z}{R(1-\nu)}\right)\left[\dfrac{r}{R}\int_0^R J_0(\gamma\rho)d\rho - \int_0^r J_0(\gamma\rho)d\rho\right] \\ u_z = \varphi(0)\exp\left(\dfrac{2\nu f z}{R(1-\nu)}\right)J_0(\gamma r) + u_0 \end{cases}$$

where J_0 is the zero order Bessel function of the first kind and γ is defined by:

(21) $$\gamma = \frac{2\nu f}{R}\sqrt{\frac{2}{(1-\nu)(1-2\nu)}}$$

The radial profile of the axial displacement $u_z(r)$ is, in fact, imposed by the relation (19). The real boundary conditions at $z=0$ and at $z=L$ may therefore not be respected exactly. The form of this solution nevertheless enables the two-dimensional effects to be taken into account.

By combining the relations (20) with Hooke's law and with the boundary conditions (9)-(10), we obtain:

(22) $$\frac{F_r}{F_m} = \exp\left(-\frac{2\nu f L}{R(1-\nu)}\right)$$

This equation demonstrates that it is possible to evaluate f from the measurements of F_m and F_r when the geometry of the problem and the Poisson coefficient of the sample are known. The form of the stresses at the interface may also be obtained (c.f. appendix):

(23) $$\begin{cases} p(z) = \dfrac{F_m \nu}{(1-\nu)\pi R^2} \exp\left(\dfrac{2\nu f (z-L)}{R(1-\nu)}\right) \\ \tau(z) = \dfrac{f F_m \nu}{(1-\nu)\pi R^2} \exp\left(\dfrac{2\nu f (z-L)}{R(1-\nu)}\right) \end{cases}$$

This confirms the heterogeneity of the interface stresses mentioned above.

3.2 An approximate solution adapted to the test

The idea is now to simplify the model to obtain a solution that takes into account the effect of the initial excess of thickness of the sample and the dependency of the friction on the normal pressure.

The approach used is similar to that of Janssen [16]. It is based on two hypotheses: (i) the tube is assumed to be perfectly rigid and (ii) the axial, radial and circumferential stresses and strains do not depend on r. This enables the problem to be approached by a one-dimensional incremental analysis, which is easier to perform.

The equilibrium equation (13) is no longer necessary and only the equilibrium equation (14) needs to be taken into account. We set: $\sigma_{zz}(r,z)=\sigma(z)$ and $\sigma_{rr}(r,z)=p(z)$. The equilibrium equation is thus:

(24) $$\frac{\partial[r\sigma_{rz}(r,z)]}{\partial r} + r\frac{d\sigma(z)}{dz} = 0$$

By integrating (24) from $r=0$ to $r=R$, we obtain:

(25) $\tau(z) = \frac{R}{2}\frac{d\sigma(z)}{dz}$ and $\sigma_{rz}(r,z) = -\frac{r}{R}\tau(z)$

The components ε_{rr} and $\varepsilon_{\theta\theta}$ are positive in compression and assumed to be independent of r. Their values are:

(26) $\varepsilon_{rr} = \varepsilon_{\theta\theta} = \frac{u_{ri}}{R}$

By applying Hooke's law, we then obtain:

(27) $\frac{Eu_{ri}}{R} = (1-\nu)p(z) - \nu\sigma(z)$

where E is the Young's modulus of the sample. It is equal to 2GPa.

The relations (9)-(10) become:

(28) $F_r = \pi R^2 \sigma(z=0)$

(29) $F_m = \pi R^2 \sigma(z=L)$

Because of the pre-tightening, a non-null force F_m is required to make the assembly slide, even if F_r is null. This force is written as F_{m0}. It is expressed as a function of the other parameters in the following form:

(30) $$F_{m0} = \frac{\left[\exp\left(\frac{2 f_0 \nu L}{R(1-\nu)}\right)-1\right]\frac{\pi E u_{ri}}{\nu}\left(R-\frac{E u_{ri}\beta}{1-\nu}\right)}{1+\frac{E u_{ri}\beta}{R(1-\nu)}\left[\exp\left(\frac{2 f_0 \nu L}{R(1-\nu)}\right)-1\right]}$$

Let Q_F and the constants Q_{F0} and Q_{F,F_r} be defined as:

(31) $$\begin{cases} Q_F = \dfrac{F_r}{F_m - F_{m0}} \\ Q_{F0} = \left[\exp\left(-\dfrac{2 f_0 \nu L}{R(1-\nu)}\right)\right]\left\{1+\dfrac{E u_{ri}\beta}{R(1-\nu)}\left[\exp\left(\dfrac{2 f_0 \nu L}{R(1-\nu)}\right)-1\right]\right\}^2 \\ Q_{F,F_r} = \dfrac{\beta\nu\left[1-\exp\left(-\dfrac{2 f_0 \nu L}{R(1-\nu)}\right)\right]\left\{1+\dfrac{E u_{ri}\beta}{R(1-\nu)}\left[\exp\left(\dfrac{2 f_0 \nu L}{R(1-\nu)}\right)-1\right]\right\}}{(1-\nu)\pi R^2} \end{cases}$$

By combining the equilibrium equation, the laws of friction, Hooke's law and the boundary conditions, we obtain the following affine relation between Q_F and F_r:

(32) $$Q_F = Q_{F0} + Q_{F,F_r} \times F_r$$

By adding the boundary conditions, we finally obtain (22). This shows that the radial independence hypothesis with respect to the axial, radial and circumferential stresses and strains has no incidence on the simultaneous evolutions of F_m and F_r and thus no incidence on the processing method.

The evolutions of F_m and F_r obtained during the tests have enabled three unknowns f_0, β and u_{ri} to be identified. Only f_0 and β are really of interest since these are the parameters

which control the behaviour of the interface. However, it is important for u_{ri} to be known thereafter in order to be able to accurately simulate the test.

Lastly, the normal and tangential stresses at the interface are determined using the following formulae:

(33)
$$\begin{cases} p(z) = \dfrac{\exp\left(\dfrac{2f_0\nu(z-L)}{R(1-\nu)}\right)}{\beta\left[\exp\left(\dfrac{2f_0\nu(z-L)}{R(1-\nu)}\right)-1\right]+\dfrac{(1-\nu)\pi R^2}{\pi REu_{ri}+\nu F_m}} \\ \tau(z) = \dfrac{f_0\left[\dfrac{(1-\nu)\pi R^2}{\pi REu_{ri}+\nu F_m}-\beta\right]\exp\left(\dfrac{2f_0\nu(z-L)}{R(1-\nu)}\right)}{\left[\beta\left[\exp\left(\dfrac{2f_0\nu(z-L)}{R(1-\nu)}\right)-1\right]+\dfrac{(1-\nu)\pi R^2}{\pi REu_{ri}+\nu F_m}\right]^2} \end{cases}$$

Similarly, when the boundary conditions are introduced into the expression of the interface stresses, equality (23) is obtained.

4 Experimental results

4.1 Performed tests

Two types of tests were performed, during one of which the strains along the tube were measured by the eight circumferential gauges (c.f. Figure 2 and Figure 3). For practical reasons, this test was performed at low pressure. The other test was performed up to a high pressure of 100MPa. Hereafter, the first test will be termed "lower pressure test" and the second "higher pressure test". The sample is merely pushed on the spring by the testing machine (c.f. Figure 2) as the measurements are taken. Thus, the normal pressure (by Poisson

effect on the sample) and the sliding are imposed simultaneously thanks to the spring stiffness (c.f. section 2.1). Both tests were carried out with the same tube and the same sample.

The measurements allow the values of the forces F_m and F_r to be accessed during loading. The raw results for both tests are presented in Figure 7. I1 properties do not vary a lot from a sample to another and friction tests are therefore reproducible. These data are then typical of several measurements.

The idea is to analytically link (using relations (30)-(31)-(32)) the friction parameters and other unknowns to magnitudes identifiable from the evolution of the two forces. This, firstly, enables the coherence of the analytical model to be verified.

An order of f relative uncertainty $\frac{\Delta f}{f}$ can be calculated from F_m relative uncertainty $\frac{\Delta F_m}{F_m}$ and from F_r relative uncertainty $\frac{\Delta F_r}{F_r}$ by introducing $u_{ri}=0$ and $\beta=0$ in relations (30)-(31)-(32), which leads to:

(34) $$\frac{\Delta f}{f} = \frac{\frac{\Delta F_r}{F_r} + \frac{\Delta F_m}{F_m}}{\left|\ln\left(\frac{F_r}{F_m}\right)\right|}$$

According to Figure 7, the $\frac{F_r}{F_m}$ ratio is around 0.4 for both tests. F_m is measured by the testing machine sensors (accuracy approx. 1N) and F_r is deduced from strain gauges (c.f.

section 2.1). As the machine sensors are very accurate $\frac{\Delta F_m}{F_m}$ can be neglected in (34), $\frac{\Delta f}{f}$ is therefore of the order of $\frac{\Delta F_r}{F_r}$ i.e. around 1%.

4.2 Analysis of the lower pressure test

Given that F_{m0}=2.81kN is obtained by the linear extrapolation of the blue curve in Figure 7, the evolution of Q_F is drawn as a function of F_r (c.f. Figure 8).

The Q_F ratio seems constant and independent of F_r. It can thus be assimilated to its mean value: Q_F=0.41. Eliminating the dependency of this ratio to F_r comes down to equating $\beta=0$ in (32), which becomes:

(35) $$f_0 = -\frac{R(1-\nu)}{2\nu L}\ln(Q_F)$$

(30) can thus be written as:

(36) $$u_{ri} = \frac{\nu F_{m0} Q_F}{\pi R E(1-Q_F)}$$

There are still two parameters remaining to be identified: u_{ri} and f_0. Since the other parameters are known, identification is made using the measured values of Q_F and F_{m0}. We deduce from (35) and (36) that u_{ri}=0.0124mm and f_0=0.167.

4.3 Analysis of the higher pressure test

For this test, the first measuring point corresponds to F_{m0} and gives F_{m0}=900N. The experimental evolution of Q_F may thus be drawn as a function of F_r (c.f. Figure 9).

The relations (30)-(31)-(32) enable the identification of the parameters f_0, β and u_{ri} based on the experimental values of the slope Q_{F,F_r} and the intercept Q_{F0} of the linear regression line and on the experimental value of F_{m0}. Since the system is difficult to be solved, an approximation is added: the initial force F_{m0} being relatively low with respect to the values attained by the forces F_m and F_r, u_{ri} is neglected with respect to the other terms in (32). The following equations are thus obtained:

(37) $$f_0 = -\frac{R(1-\nu)}{2\nu L}\ln(Q_{F0})$$

(38) $$\beta = \frac{(1-\nu)\pi R^2 Q_{F,F_r}}{\nu(1-Q_{F0})}$$

A linear regression leads to Q_{F0}=0.339 and Q_{F,F_r} =0.00223kN^{-1}. Since the other parameters are known, f_0=0.203 and β=0.00159MPa^{-1} can be deduced.

In relation (30), the second order terms at u_{ri} are neglected and by taking relation (37) into account, we obtain:

(39) $$u_{ri} = \frac{\nu F_{m0} Q_{F0}}{\pi R E(1-Q_{F0})}$$

(39) gives u_{ri}=0.00294mm.

The system of relations (33) and the numerical simulations (c.f. section 5.1) enable the contact pressures to be estimated at the interface, whereas these are not able to be measured. It is thus possible to account for the pressure ranges covered during this test (c.f. Figure 10).

The friction coefficients identified during the two tests are not quite equal. At a pressure of 30MPa, the first test gives a coefficient of 0.17 and the second one a coefficient of 0.19. The interface conditions change over time (polishing of the sample, smoothing of any asperities of the steel, etc) since these tests are performed successively with the same tube and the same sample, the assembly being simply put back into position after each test. The lower pressure test being performed after the higher pressure test, the reduction in friction between the two tests can be explained by the changing interface conditions. Moreover, the sliding rates imposed during the lower pressure test are of a magnitude of a mm/h whereas they are of a magnitude of a mm/min for the high pressure test. This change may also have an effect.

The value of the friction coefficient reduces when the contact pressure increases, as suggested by certain authors [2]. For the example shown here, this value goes from 0.2 at very low contact pressure to 0.16 at contact pressure of 140MPa.

5 Simulations and discussion

The tests were numerically simulated to validate the analysis and the friction parameters thus identified.

Modelling was performed using the finite element method. The software used was ABAQUS CAE / Standard (implicit). The performed calculations were two-dimensional and axisymmetric. Quadrangular elements with quadratic interpolation were used. All the normal contacts were defined by "hard contact" "direct contact" (no interpenetration), separation being allowed (no bonding). The tangential contact between the confinement tube and the sample obeys a Coulomb's law (the coefficient being an affine function of the pressure) imposed using the method of Lagrange multipliers. The other tangential contacts are without friction.

The mechanical properties selected for the steel and the aluminium were respectively a Young's modulus of 210GPa and a Poisson coefficient of 0.33, and a Young's modulus of 74GPa and a Poisson coefficient of 0.3. The sample behaviour is assumed to be perfectly elastic with a 2GPa Young's modulus (c.f. section 3.2) and a 0.4 Poisson coefficient (c.f. section 2.2). This assumption will be checked in section 5.4.

The finite elements are squares of 1mm in length. There are therefore 10 elements in the radius of the sample.

5.1 Validity of the analysis method

The test was simulated with the parameters determined during the analysis. Numerical simulation enables the evolutions of F_m and F_r (and thus of Q_F) to be obtained as well as the interface stress profiles (which is to say $p(z)$ and $\tau(z)$). Thereafter, the results were compared with those obtained experimentally.

For the lower pressure test, loading was simulated with F_m rising up to F_m^{MAX}=17kN (which is equal to the maximal F_m experimentally reached). The parameters identified from the model allow the finite element evolution of Q_F as a function of F_r to be very close to the experimental one (c.f. Figure 8). The friction parameter identification technique is thus validated. Figure 11 shows that our approach cannot be used to predict boundary effects, but this has no incidence on the identification of the friction parameters.

For the higher pressure test, loading was simulated with F_m rising up to F_m^{MAX}=75kN (which is equal to the maximal F_m experimentally reached). The conclusions regarding the numerical simulation of the higher pressure test are exactly the same as previously (c.f. Figure 9 and Figure 11).

Figure 12 displays (for the higher pressure test) that the radial pressure field is homogenous in the radial direction everywhere in the sample but near the top and bottom boundaries.

Despite its imperfections, the model enables the simultaneous evolutions of the magnitudes Q_F and F_r to be accurately obtained, and this for both tests. Q_F and F_{m0} are both calculated with f_0=0.167, β=0 and u_{ri}=0.0124mm using relations (30)-(31)-(32), using the simulation of the lower pressure test and using an additional simulation considering a rigid tube. The results (c.f. Table 1) show that the slight deviations between the model and the simulations are actually due to the flexibility of the tube which is not taken into account in the model. Indeed, the relative deviations between the model and the simulation are higher than those between the model and the simulation considering a rigid tube.

The numerical simulations enable the validity of the analysis, and thus the validity of the friction parameters thereby defined, to be ensured.

5.2 Consistency of superabundant measurements

During a test, the circumferential strain profile along the tube $\varepsilon_{\theta\theta}(z)$ was measured at several steps during the loading, that is to say at several values of the force F_m. A discrete experimental profile was obtained and compared with the numerically obtained profile so as to verify their consistency. Figure 13 shows the position and width of each of the gauges as well as their measurements.

With the exception of the values obtained at $z=L$, a satisfactory correspondence is to be noted between the experimental and numerical axial profiles (c.f. Figure 13).

The higher pressure test was performed at a higher loading rate. For practical reasons, only the strain of the gauge glued at $z=0.5L$ was measured (c.f. Figure 14).

Despite some imperfections, no significant deviations were observed between the simulated strains and the measured ones, thereby providing an additional guarantee with regard to the consistency of the method.

5.3 Influence of the friction at the top and bottom boundaries

The interface conditions at the top and bottom boundaries (located at $z=0$ and at $z=L$) may have an influence on the behaviour of the sample, in particular during the tests on the Hopkinson bars [12], [18], [25]. It is thus necessary to ensure that these effects remain negligible with the selected configuration (slender sample with radial confinement).

For this, the numerical results obtained for two extreme cases were compared. The results presented in sections 5.1 and 5.2 were obtained by modelling the contacts at the top and bottom boundaries without friction (the friction coefficient being assumed to be null). The simulations were performed again but with changed boundary conditions: instead of imposing a null friction stress at the boundaries, contacts with null relative displacement were imposed (friction coefficient being assumed to be infinite).

We observed that the friction coefficient value at the top and bottom boundaries has no influence (relative deviation of less than 2%) on the evolution of Q_F as a function of F_r, and thus no influence on the parameters identified during the analysis.

5.4 Verification of the elasticity hypothesis

The elasticity hypothesis of the sample had to be verified to ensure the consistency of the analysis. The criterion $(\sigma_{mises}-\alpha P)$ was calculated in the sample during the numerical simulations and this after the loading when the forces were maximal. Thereafter, the fulfilment of the condition $(\sigma_{mises}-\alpha P)<C$ (where α=0.64 and C=25MPa) is verified.

The numerical results obtained for the two extreme cases at the boundaries (null friction coefficient, infinite friction coefficient) were compared. These calculations were performed only for the higher pressure test for which the stresses are the highest.

The value of the criterion was at most 13MPa; this remains therefore within the elastic domain (c.f. Figure 16).

The simulations were performed once again but by imposing an infinite friction coefficient at the top and bottom boundaries. Loading was also simulated with F_m rising up to F_m^{MAX}=75kN.

The value of the criterion was at most 5.1MPa; this remains therefore within the elastic domain (c.f. Figure 17).

The values attained by the criterion $(\sigma_{mises}-\alpha P)$ depend on the contact conditions at the boundaries. In the two envisaged extreme cases, we observed that the elastic limit C was never attained. Our analysis, which uses an elastic solution, is therefore valid. Significantly, the criterion $(\sigma_{mises}-\alpha P)$ is only positive in very localized areas.

The sample is forced into the tube by using the testing machine. Numerical simulations of this insertion display that (2) remains satisfied for the lower and the higher pressure test. As a result, no plastic deformations take place during insertion.

6 Conclusion

This article presents a new experimental test for friction between steel and a brittle material. A technique from the compacting of granular materials is used so as to maintain the integrity of the brittle material under high interface pressures.

The analysis, performed analytically and numerically, enables the friction parameters to be obtained and shows that pressures of around 100MPa are reached. The simulations also show that the sample does not fracture under the load to which it is subjected. The developed assembly thus enables pressures with higher magnitudes than in [5] and [13] to be attained without any deterioration of the material. The sliding rates imposed at the interface are of an order of magnitude of a mm/min (higher pressure test) and a mm/h (lower pressure test). The measured friction coefficient is of around 0.2. The device enables the variation of this coefficient to be quantified when the contact pressure increases.

The device enables something to be made to slide under high contact pressure, and the method has been validated. Test campaigns may be undertaken on inert or reactive materials. The dispersion aspect of the parameters identified may be understood.

One alternative to the analysis technique would be the used of an inverse method. The feasibility of such a method is shown in [7].

The next stage of the study is to mount the experimental device on a system of Hopkinson bars so as to reach sliding rates of an order of magnitude of 10m/s.

Appendix

By using the form of u_z defined in relation (19), relation (18) produces the solution:

(A1) $$\varphi(z) = \varphi(0)\exp\left(-\frac{f'(R)(1-2\nu)}{f(R)2\nu f}z\right)$$

and then, relation (17) becomes:

(A2) $$\frac{f'(r)+rf''(r)}{rf(r)} = -\frac{(1-\nu)(1-2\nu)}{2\nu^2 f^2}\left[\frac{f'(R)}{f(R)}\right]^2$$

If we set:

(A3) $$\gamma = -\sqrt{\frac{(1-\nu)(1-2\nu)}{2}}\frac{f'(R)}{f(R)\nu f}$$

The form of *f(r)* is deduced from (A2) and this gives:

(A4) $$u_z(r,z) = \varphi(0)\exp\left(\gamma\sqrt{\frac{1-2\nu}{2(1-\nu)}}\times z\right)J_0(\gamma r) + u_0$$

where J_0 is the zero order Bessel function of the first kind.

The relation (16) enables $u_r(r,z)$ to be determined in the form defined by (19). Taking (12) into account, we then obtain:

(A5) $$\psi(z) = \frac{\gamma\varphi(0)}{2(1-\nu)}\sqrt{\frac{1-2\nu}{2(1-\nu)}}\exp\left(\gamma\sqrt{\frac{1-2\nu}{2(1-\nu)}}\times z\right)$$

(A6) $$g(r) = \frac{r}{R}\int_0^R J_0(\gamma\rho)d\rho - \int_0^r J_0(\gamma\rho)d\rho$$

The equation (A3) enables the value of γ to be determined. To solve this equation, a hypothesis is first posed, then verified a posteriori: the terms at $(\gamma R)^n$ where $n \geq 3$ are assumed to be negligible and the Bessel functions at γR and at γr can be assimilated to their limited development of the second order. In this case we obtain:

(A7) $$\frac{f'(R)}{f(R)} = \frac{-\gamma J_1(\gamma R)}{J_0(\gamma R)} = -\frac{\gamma}{2}(\gamma R) + o\left((\gamma R)^2\right) \approx -\frac{\gamma^2 R}{2}$$

where J_1 is the first order Bessel function of the first kind.

The equation (A3) is thus easily solved, and we obtain:

(A8) $$\gamma R = 2\nu f\sqrt{\frac{2}{(1-\nu)(1-2\nu)}}$$

To ensure the consistency of the approach, the accuracy of the approximation (A7) must be evaluated. For this, we must calculate the relative error *err* committed as a function of the value of the friction coefficient *f*.

(A9) $$err = \frac{\left(\frac{-\gamma J_1(\gamma R)}{J_0(\gamma R)}\right) - \left(-\frac{\gamma^2 R}{2}\right)}{\left(\frac{-\gamma J_1(\gamma R)}{J_0(\gamma R)}\right)}$$

By substituting the expression given by (A8), we obtain:

$$(A10)\quad err = \frac{\frac{J_1}{J_0}\left(2\nu f\sqrt{\frac{2}{(1-\nu)(1-2\nu)}}\right) - \nu f\sqrt{\frac{2}{(1-\nu)(1-2\nu)}}}{\frac{J_1}{J_0}\left(2\nu f\sqrt{\frac{2}{(1-\nu)(1-2\nu)}}\right)}$$

According to Figure 18, the approximation (A7) remains valid for the usual values of the friction coefficient *f*.

The formulae (23) are determined on the basis of Hooke's law, neglecting u_r and $u_{r,r}$ and applying the approximation (A7).

References

[1]: Bailly P, Delvare F, Vial J, Hanus JL, Biessy M, Picart D. Dynamic behavior of an aggregate material at simultaneous high pressure and strain rate: SHPB triaxial tests. International Journal of Impact Engineering, 38, 73-84, 2011.

[2]: Ben-Dor G, Dubinsky A, Elperin T. Localized interaction models with non-constant friction for rigid penetrating impactors. International Journal of Solids and Structures 44, 2593-2607, 2007.

[3]: Bruska Azhdar, Bengt Stenberg, Leif Kari. Determination of dynamic and sliding friction, and observation of stick-slip phenomenon on compacted polymers during high velocity compaction. Polymer Testing 25, 1069-1080, 2006.

[4]: Burlion N, Pijaudier-Cabot G, Dahan N. Experimental analysis of compaction of concrete and mortar. Int. J. Num. Anal. Methods Geomech., 25(15), 1467-1486, 2001.

[5]: Dickson PM, Parker GR, Smilowitz LB, Zucker JM, Asay BW. Frictional Heating and Ignition of Energetic Materials. CP845, Conference of the American Physical Society Topical Group on Shock Compression of Condensed Matter, 1057-1060, 2005.

[6]: Durand B, Delvare F, Bailly P, Picart D. Caractérisation du comportement à l'interface entre un matériau agrégataire et un acier sous forte pression et à grande vitesse. 20ième Congrès Français de Mécanique, 2011a, (in french).

[7]: Durand B, Delvare F, Bailly P. Numerical solution of Cauchy problems in linear elasticity in axisymmetric situations. International Journal of Solids and Structures, 21, 3041-3053, 2011b.

[8]: Field JE, Swallowe GM, Heaven SN. Ignition mechanisms of explosives during mechanical deformations. Proc Roy Soc London A 1982; 383: 231-44.

[9]: Forquin P, Arias A, Zaera R. An experimental method of measuring the confined compression strenght of geomaterials. International Journal of Solids and Structures, 44, 4291-4317, 2007.

[10]: Forquin P, Safa K, Gary G. Influence of free water on the quasi-static and dynamic of strength of concrete in confined compression tests. Cement and Concrete Research, 40, 321-333, 2009.

[11]: Gruau C, Picart D, Belmas R, Bouton E, Delmaire-Sizes F, Sabatier J, Trumel H. Ignition of a confined high explosive under low velocity impact. International Journal of Impact Engineering, 36, 537-550, 2008.

[12]: Hartley RS, Cloete TJ, Nurick GN. An experimental assessment of friction effects in the split Hopkinson pressure bar using the ring compression test. International Journal of Impact Engineering, 34, 1705-1728, 2007.

[13]: Hoffman, Chandler JB, Aspect of the tribology of the plastic bonded explosive LX-04. Propellants, Explosives, Pyrotechnics, 29, 368-373, 2004.

[14]: Huang H, Feng R. Dynamic tribological response of SiC fracture surfaces. Mechanics of Materials, 38, 186-202, 2006.

[15]: Huang H, Feng R. Dynamic Friction of SiC Surfaces: A Torsional Kolsky Bar Tribometer Study. Tribology Letters, 27, 329-338, 2007.

[16]: Janssen HA, Ver Z. Dsch. Ing. 39, 1045 (1895).

[17]: Kim HJ, Emge A, Winter RE, Keightley PT, Kim WK, Falk ML, Rigney DA. Nanostructures generated by explosively driven friction: Experiments and molecular dynamics simulations. Acta Materiala, 57, 5270-5282, 2009.

[18]: Li QM, Lu YB, Meng H. Further investigation on the dynamic compressive strength enhancement of concrete-like materials based on split Hopkinson pressure bar tests. International Journal of Impact Engineering, 36, 1335-1345, 2009.

[19]: Philippon S, Sutter G, Molinari A. An experimental study of friction at high sliding velocities. Wear, 257, 777-787, 2004.

[20]: Picart D, Delmaire-Sizes F, Gruau C, Trumel H. Ignition of a HMX-based PBX submitted to impact: strain localisation and boundary condition. 16th Conference of the American Physical Society Topical Group on Shock Compression of Condensed Matter, 2009.

[21]: Picart D, Bouton E. Non-shock ignition of a HMX-based high explosive: thermo-mechanical numerical study. 14th Int Detonation Symp, Coeur d'Alène (USA), 11-16/04/2010.

[22]: Rajagopalan S, Irfan MA, Prakash V. Novel experimental techniques for investigating time resolved high speed friction. Wear, 225-229, 1222-1237, 1999.

[23]: Rajagopalan S, Prakash V. An experimental method to study high speed sliding characteristics during forward and reverse slip. Wear, 249, 687-701, 2001.

[24]: Vandersall KS, Chidester SK, Forbes JW, Garcia F, Greenwood DW, Switzer LL, et al. Experimental and modeling studies of crush, puncture, and perforation scenarios in the Steven impact test. In: Office Naval Research ONR 333-05-02, editors. Proc. 12th international detonation symposium; San Diego: 2002 pp. 131-139.

[25]: Walley SM, Church PD, Furth M, Field JE. A high-speed photographic study of the rapid deformation of metal annuli: comparison of theory with experiment. J. Phys IV France 7 (1997). Colloque C3, Supplément au Journal de Physique III d'août 1997, 317-322.

[26]: Wiegand DA, Redingius B, Ellis K, Leppard C. Pressure and friction dependant mechanical strength - cracks and plastic flow. International Journal of Solids and Structures 48, 1617-1629, 2011.

[27]: Yong-Ming Tien, Po-Lin Wu, Wei-Hsing Huang, Ming-Feng Kuo, Chen-An Chu. Wall Friction measurement and compaction characteristics of bentonite powders. Powder Technology 173, 140-151, 2007.

	relations (30)-(31)-(32)	simulation (rigid tube)	simulation
Q_F (relative deviation)	0.410	0.408 (-0.49%)	0.421 (2.7%)
F_{m0} (relative deviation)	2.80kN	2.83kN (1.1%)	2.68kN (-4.3%)

Table 1: Q_{F0} and F_{m0} calculated with f_0=0.167, β=0 and u_{ri}=0.0124mm and relative deviations between analytical relations and simulations.

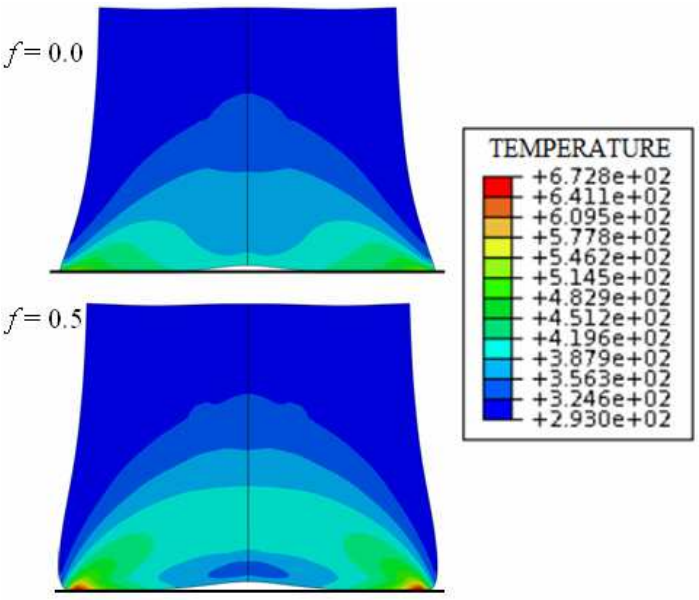

Figure 1: Numerical simulation of the heating of an explosive projected at 100m/s against a rigid wall. Temperature in Kelvin 30µs after impact when the friction coefficient *f* is 0.0 and 0.5.

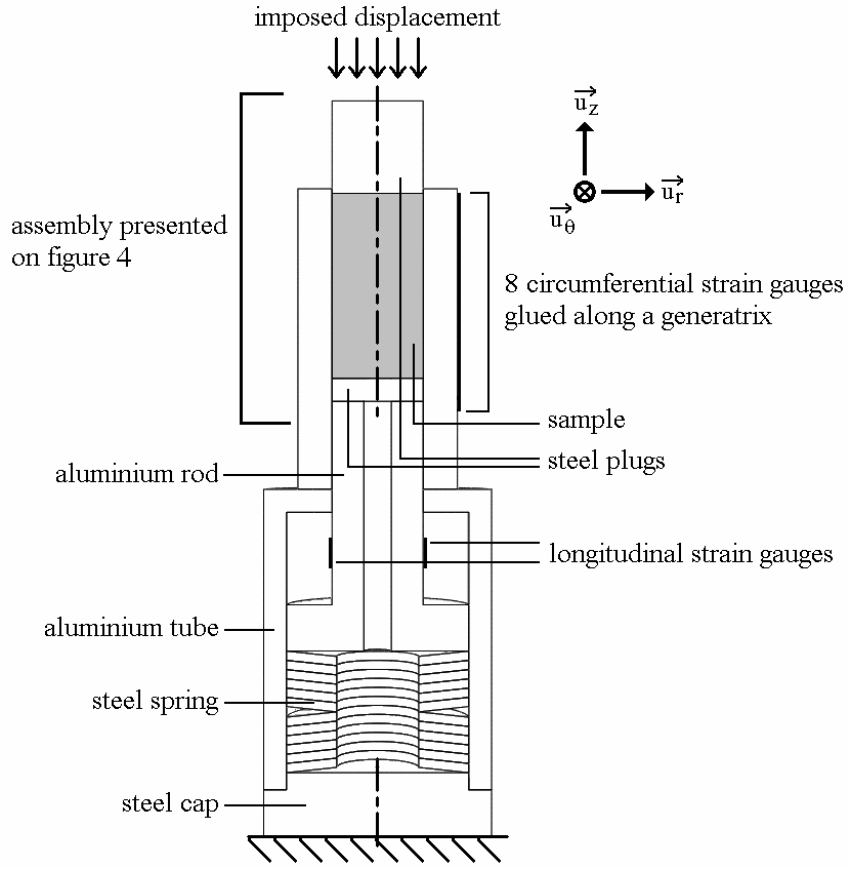

Figure 2: Diagram of the device placed in a testing machine. The sample is 20mm in diameter and 40mm in height. The external diameter of the tube is of 34mm. The radial clearance between the steel plugs and the steel confinement tube is roughly equal to 10^{-2}mm.

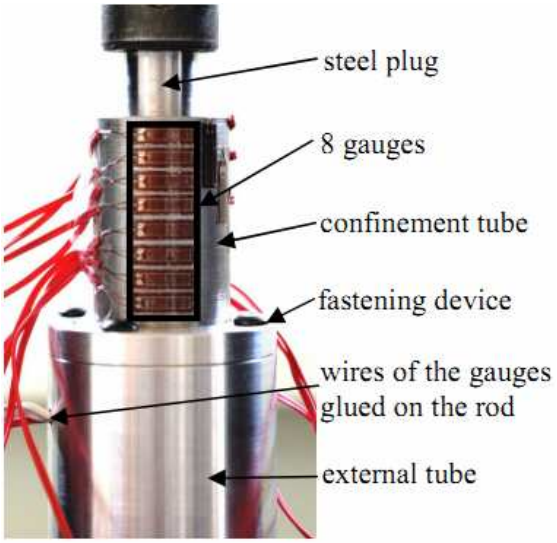

Figure 3: Photograph of the device placed in a testing machine.

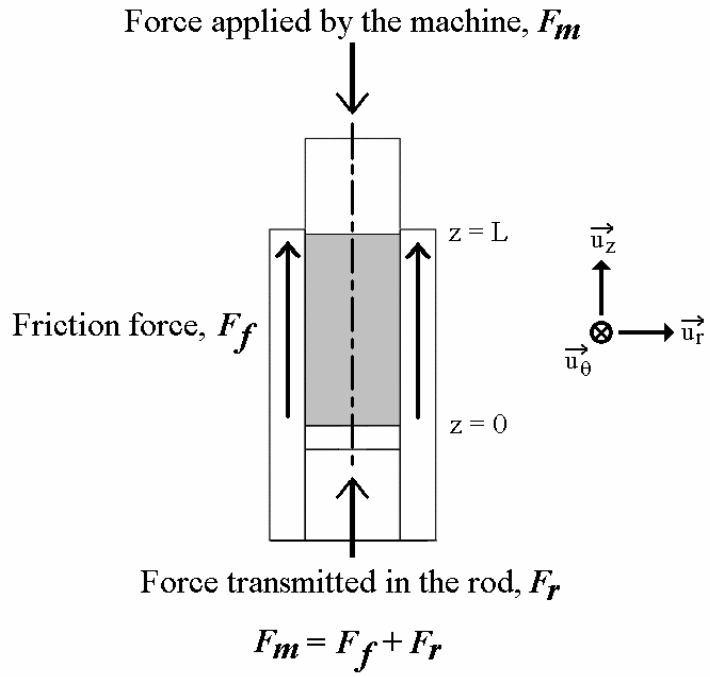

Figure 4: Definition of the forces on the assembly.

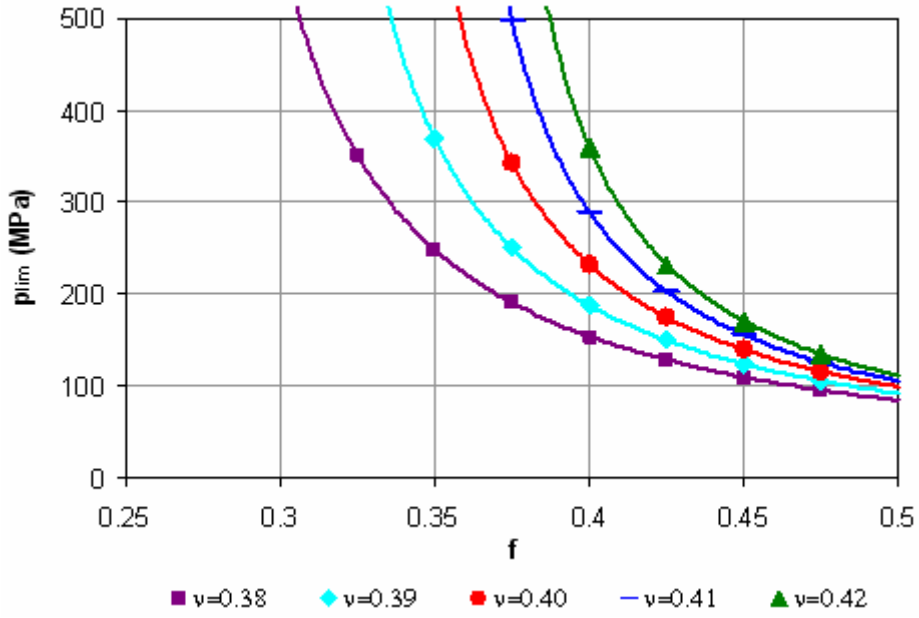

Figure 5: Evolution of p_{lim} as a function of f for different values of ν.

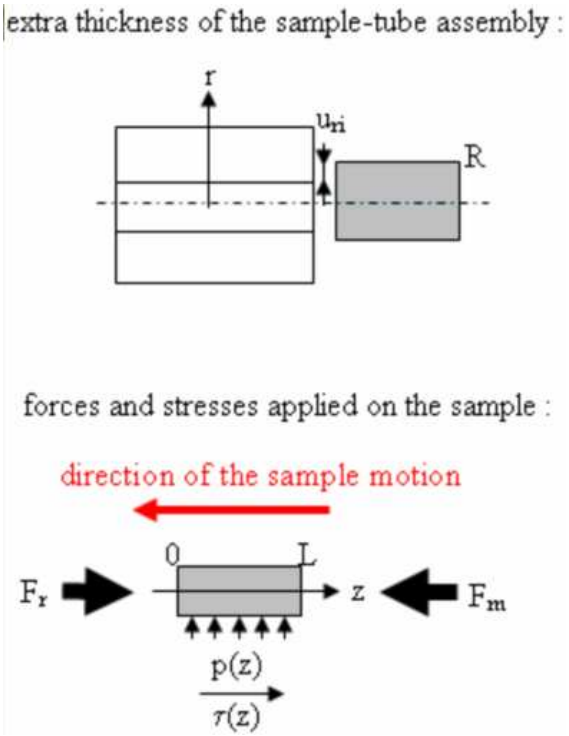

Figure 6: Definition of the mechanical problem.

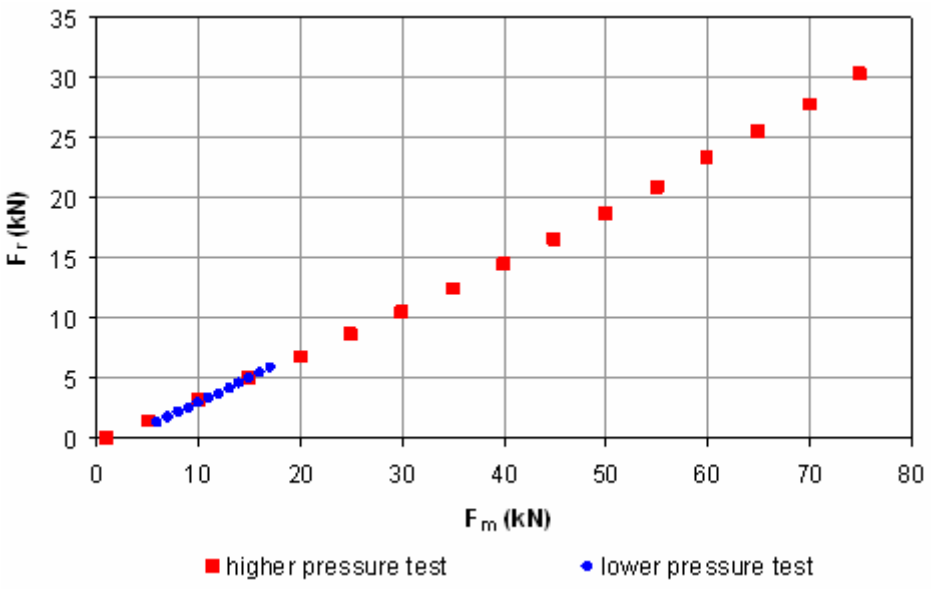

Figure 7: Comparison of the evolutions of F_r as a function of F_m during the two tests.

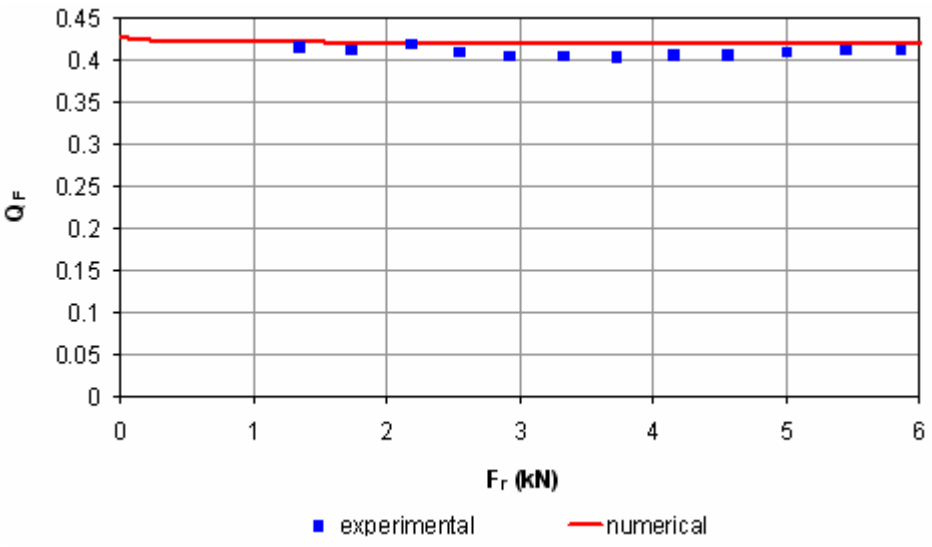

Figure 8: Experimental evolution of Q_F as a function of F_r for the lower pressure test (blue).

Result of the finite element simulation (red) detailed in section 5.

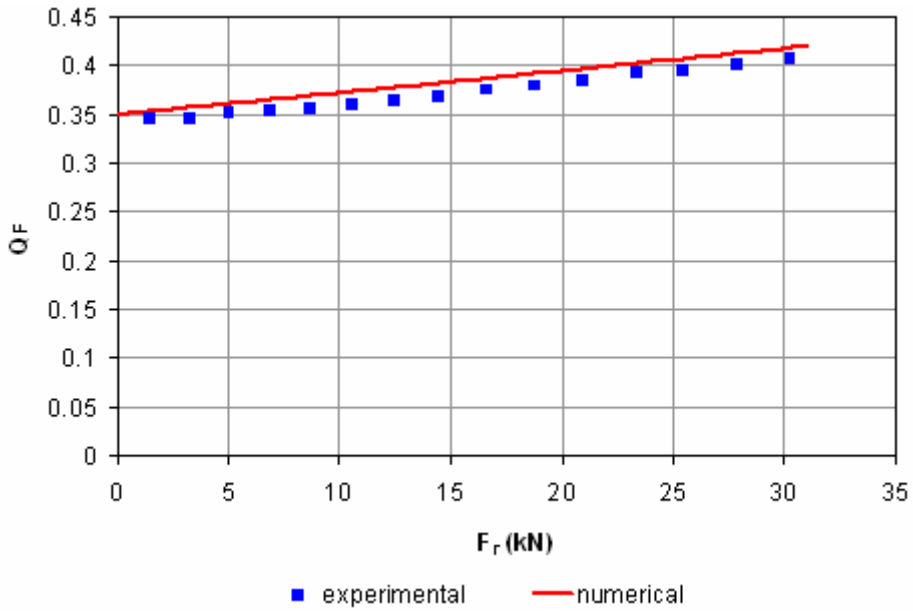

Figure 9: Experimental evolution of Q_F as a function of F_r for the higher pressure test (blue). Result of the numerical simulation detailed in section 5 (red).

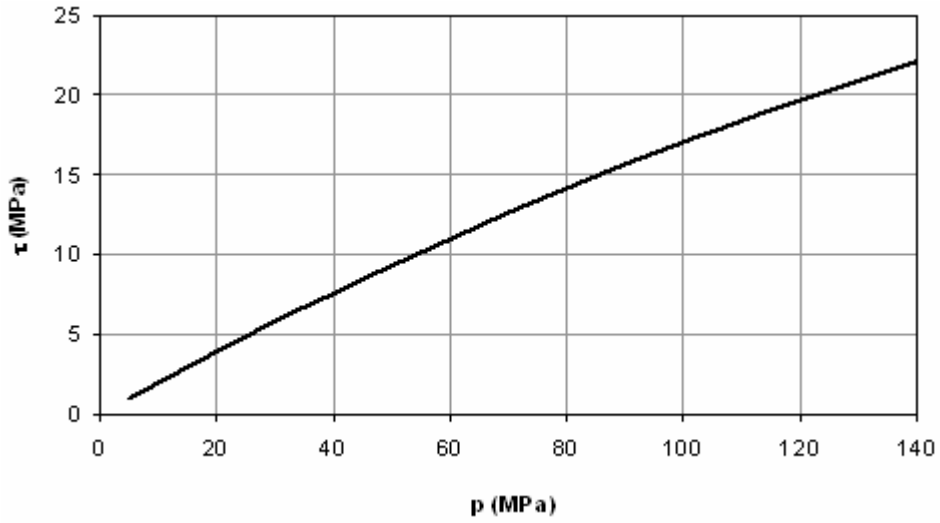

Figure 10: Friction law identified using the higher pressure test (pressure range between 5 and 140MPa).

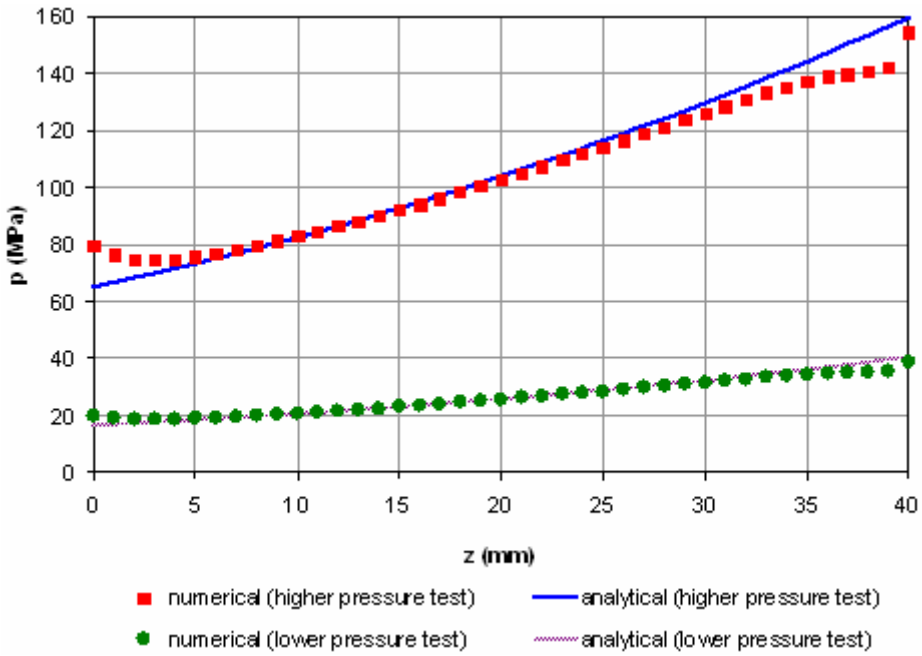

Figure 11: Comparison of the analytical and numerical profiles of pressure *p(z)* for both tests when the force is maximal ($F_m=F_m^{MAX}$).

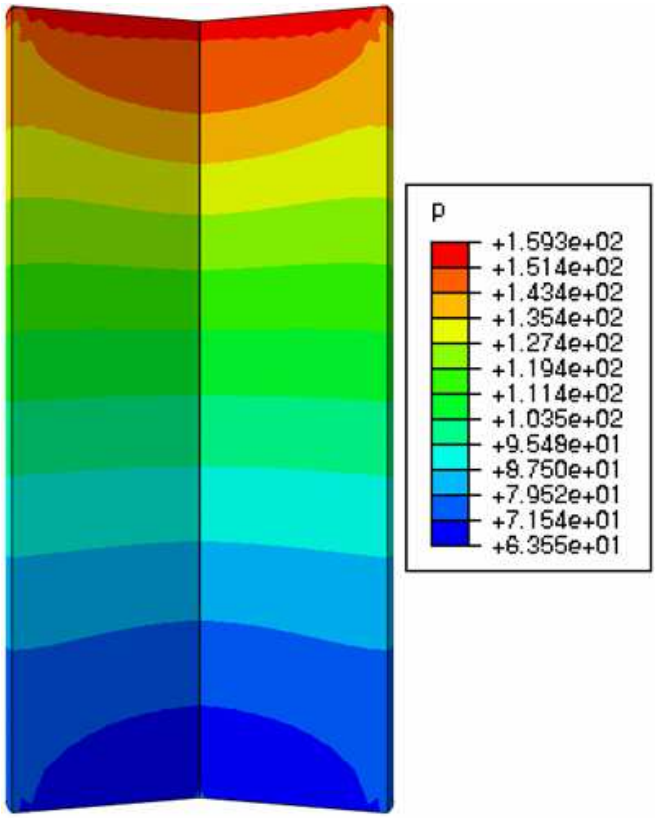

Figure 12: Value of the radial pressure *p* in MPa for the higher pressure test.

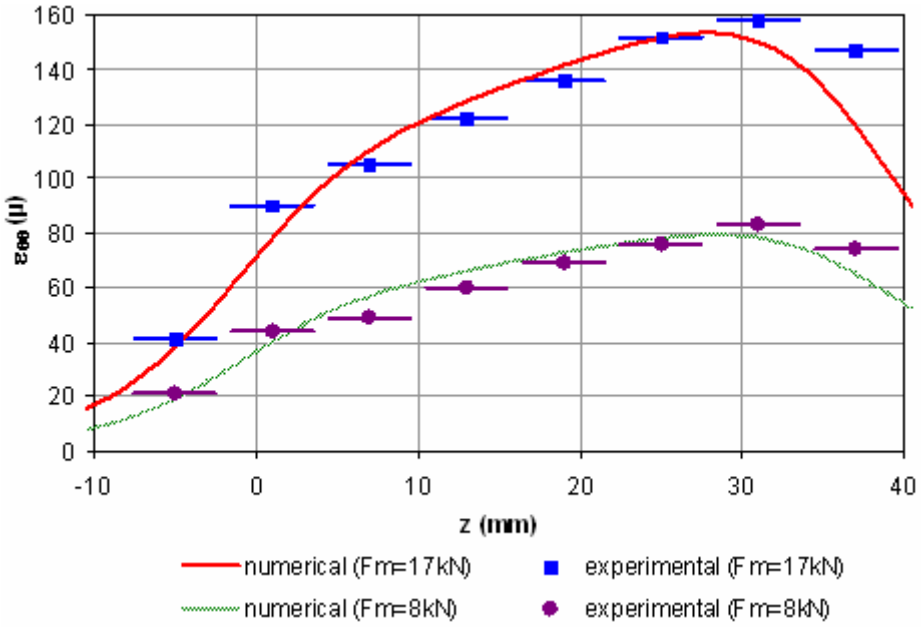

Figure 13: Comparison of the experimental and numerical profiles of $\varepsilon_{\theta\theta}(z)$ for two values of F_m during the lower pressure test.

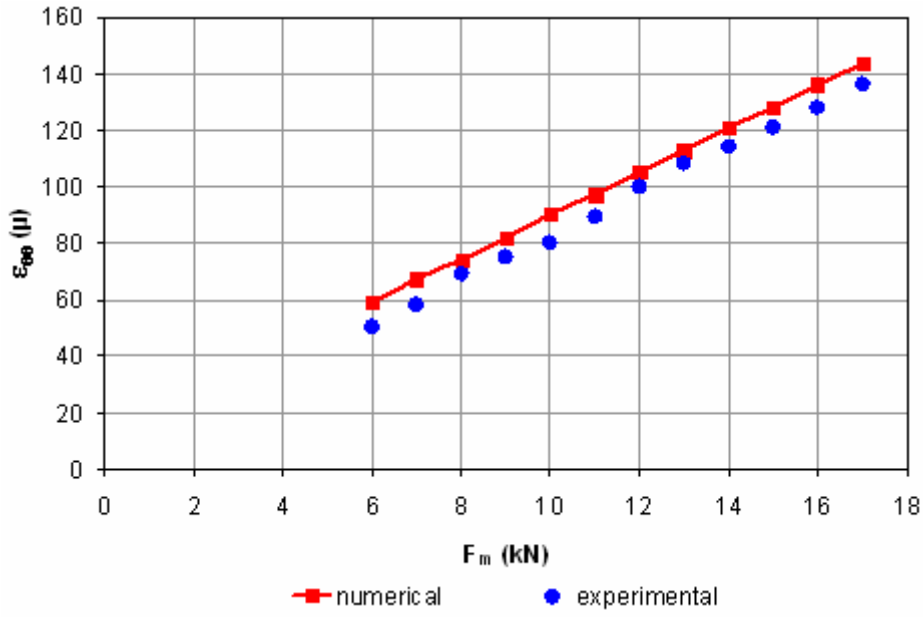

Figure 14: Comparison of the experimental and numerical evolutions of $\varepsilon_{\theta\theta}(z=0.5L)$ as a function of F_m for the lower pressure test.

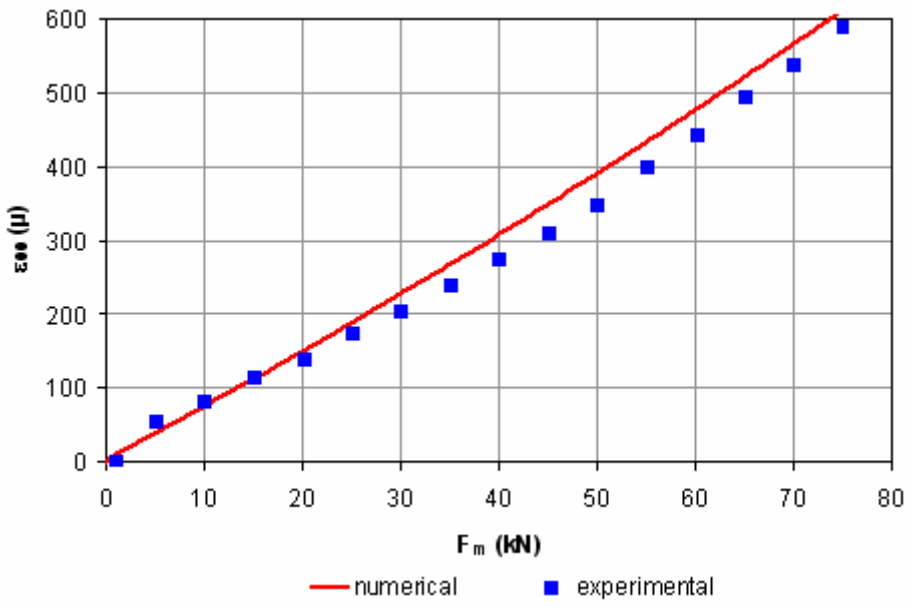

Figure 15: Comparison of the experimental and numerical evolutions of $\varepsilon_{\theta\theta}(z=0.5L)$ as a function of F_m for the higher pressure test.

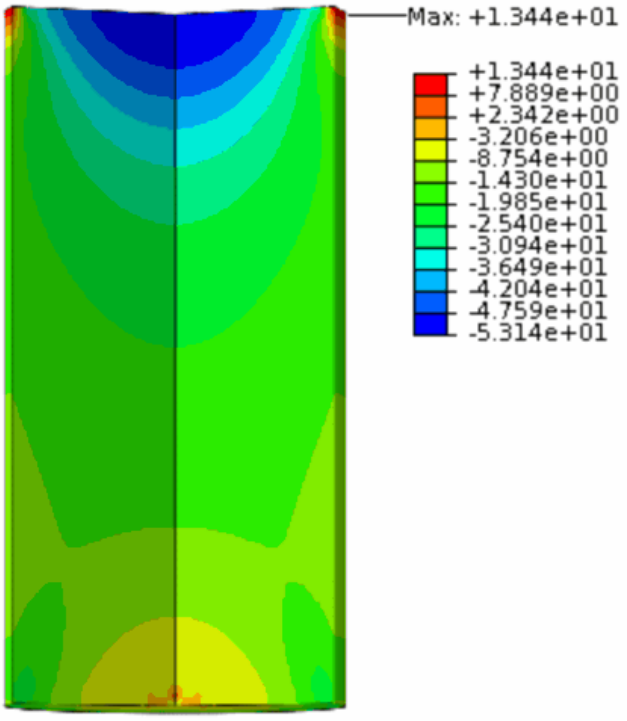

Figure 16: Value of the criterion $(\sigma_{mises}-\alpha P)$ in MPa after the loading for the higher pressure test and in the hypothesis of a null friction coefficient at the top and bottom boundaries.

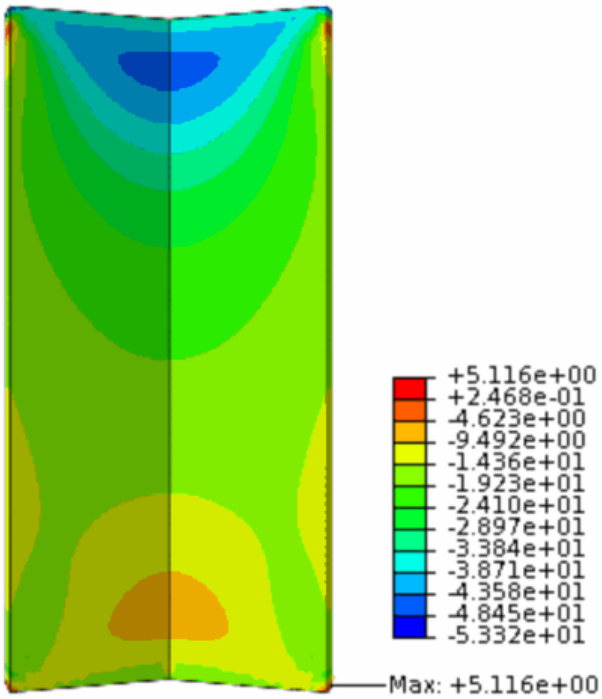

Figure 17: Value of criterion $(\sigma_{mises}-\alpha P)$ in MPa after the loading for the higher pressure test and in the hypothesis of an infinite friction coefficient at the top and bottom boundaries.

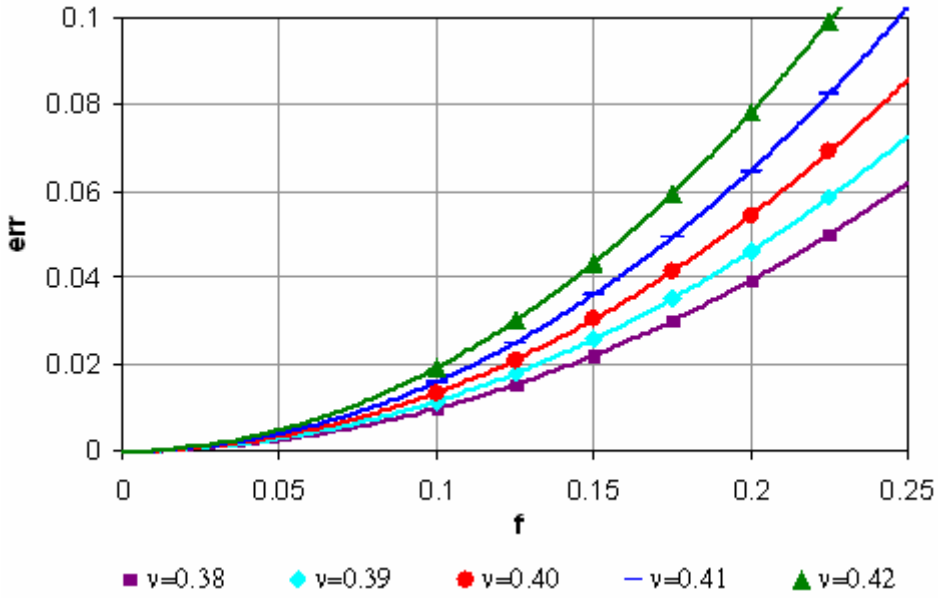

Figure 18: Evolution of the relative error *err* as a function of the friction coefficient *f*.